Silicon Photonic IQ Modulators for 400 Gb/s and beyond

Hassan Sepehrian, Jiachuan Lin, Leslie A. Rusch and Wei Shi

Silicon Photonic IQ Modulators for 400 Gb/s and beyond

Hassan Sepehrian, *Student member, IEEE*, Jiachuan Lin, *Member, IEEE*, Leslie A. Rusch, *Fellow, IEEE* and Wei Shi, *Member, IEEE*

Abstract—Silicon photonics has enormous potential for ultra-high-capacity coherent optical transceivers. We demonstrate an IQ modulator using silicon photonic traveling-wave modulators optimized for higher-order quadrature amplitude modulation (QAM). Its optical and RF characteristics are studied thoroughly in simulation and experiment. We propose a system-orientated approach to optimization of the silicon photonic IQ modulator, which minimizes modulator-induced power penalty in a QAM transmission link. We examine the trade-off between modulation efficiency and bandwidth for the optimal combination of modulator length and bias voltage to maximize the clear distance between adjacent constellation points. This optimum depends on baud rate and modulation format, as well as achievable driving voltage swing. Measured results confirm our prediction using the proposed methodology. Without pre-compensating bandwidth limitation of the modulator, net data rates up to 232 Gb/s (70 Gbaud 16-QAM) on single polarization are captured, indicating great potential for 400+ Gb/s dual-polarization transmission.

Index Terms— Silicon Photonics, IQ modulator, traveling-wave optical modulator, quadrature amplitude modulation (QAM), modulator power penalty.

I. INTRODUCTION

THE growing demand for ultra-fast optical links has created intense interest in low-cost, integrated transceivers. This is one of the major driving forces for research in silicon photonics (SiP) [1,2]. Silicon has numerous advantages over other platforms (e.g., LiNbO3 and InP), such as its compatibility with the CMOS fabrication process and the ability to manipulate polarization on a chip. However, high-performance optical modulation in silicon is in general more challenging.

Despite recent demonstrations in higher-order modulation formats, with direct detection [2-6] or coherent detection [7-10], there exists a gap between optimization efforts in the design of SiP modulators and in the system-level performance. A joint optimization, of both modulator design and system parameters, could further push performance. Most of the previously reported works [2] focused on maximizing the electro-optic bandwidth of the modulator (BW_{E-O}) or on increasing the modulation efficiency by lowering modulator V_π

(to make it more compatible with small-swing CMOS drivers).

Next-generation coherent optical transceivers, targeting 400 Gb/s and beyond, are under active research and development. For a given baud rate (usually limited by the driver swing or BW_{E-O}), higher-order modulation can increase bit rate; these modulation formats (i.e., 2^N-QAM, where N is the number of bits per symbol) require, however, very high optical signal-to-noise ratios (OSNR).

For a fixed receiver noise level contributing to OSNR, the amplitude of the modulated signal determines the SNR performance. When it comes to modulator design, we want to minimize the modulator induced power penalty. In [11], the authors guide modulator design by seeking to maximize the optical modulation amplitude (OMA) of the transmitter for multi-level pulse amplitude modulation (PAM-M). This system-orientated approach focuses on the power-penalty induced by the modulator and optimizes the modulator design to increase the eye openings in a multi-level modulation format, with the expectation of improved bit error rate (BER).

Three main factors affect the output of the modulator and limit the signal quality: optical loss, modulation loss (coming from limited extinction ratio due to high V_π), and inter-symbol interference (ISI) induced by limited electro-optic modulator bandwidth. These three penalty sources are intricately intertwined. Minimizing each of them separately does not necessarily minimize the overall modulator-induced penalty. Considering these limiting factors, a new bandwidth aware figure of merit has been proposed for optimizing the design or bias point of a SiP MZM for a specific baud rate in PAM-M modulation [11].

For a given foundry process, the design of a Mach-Zehnder modulator (MZM) per unit length can be optimized following the process specifications and design rules. However, we must optimize the length and the bias voltage of the phase shifter for the system context (e.g., for a target baud rate and modulation format). In this paper, we propose a new design procedure minimizing the modulator-induced power penalty for QAM transmission. We demonstrate an integrated in-phase and quadrature (IQ) modulator following this design procedure and using depletion-mode silicon phase shifters based on a 220-nm SiP foundry process.

We target 16-QAM at 60 Gbaud to achieve 200 Gb/s per channel for a single polarization. To verify the proposed optimization approach experimentally, we isolate the SiP modulator imperfections from other transmitter impairments (e.g., from the digital to analogue converter (DAC)). We do not

pre-compensate for the limited bandwidth of the modulator. We push the baud rate up to 70 Gbaud, despite exceeding the device bandwidth, to probe the device capacity.

The rest of this paper is organized as follows. In Section II, we present a general, unit-length MZM design and its optical and electrical characteristics. Section III optimizes the IQ modulator design. We examine power penalties induced by a SiP IQ modulator in a QAM transmission link; using the optical and electrical characteristics extracted in Section II. We identify the optimal combination of length and bias voltage of the phase shifter, that is, the combination that gives the minimum total modulator-induced power penalty. We found, via simulation, a constraint on IQ branch separation to avoid RF crosstalk between the branches. In section IV, our experiment setup and measured results are presented. Finally, Section V concludes this paper.

II. DESIGN AND CHARACTERISTICS OF TW-MZM

Figure 1 presents a schematic of the SiP IQ modulator that consists of a pair of MZMs nested in an MZ interferometer. Each MZM uses a phase shifter employing lateral p-n junction and a traveling-wave (TW) electrode for high-frequency operation. The TW-MZM is driven in a series push-pull configuration. A negative voltage is applied between the two arms of each MZM; thus, the phase shifter works in the depletion mode.

A. TW-MZM Design

Figure 2a shows the cross-sectional schematic of the SiP TW-MZM (identical for I and Q) using a CMOS-compatible process (A∗STAR IME, Singapore) on a 220-nm SOI wafer with 2 μm buried oxide. The phase shifter applies a lateral p-n junction embedded in the centre of a rib waveguide. While highly doped P++ and N++ regions are used for ohmic contacts, intermediate P+ and N+ doping levels are used to reduce the series resistance without significantly increasing optical propagation loss.

The phase shifter can be modeled as a series of lumped capacitors and resistors [5,11], whose values depend on the applied voltage. We conduct 2D simulation in Lumerical Mode and Device software at wavelength λ =1550 nm to predict the electro-optic response of the phase shifter and to calculate the circuit components. Figure 2b shows the calculated junction capacitance (C_j) and resistance (R_j). We calculate the overlap between the optical mode and the carrier distribution to predict the changes in refractive index, Δn_{eff}, and loss as functions of reverse voltage, as shown in Fig. 2c. More details can be found in [11].

As shown in Fig. 3a, the TW electrode has a coplanar stripline (CPS) configuration loaded by the p-n junction. For velocity matching between optical waves and RF driving signals, the RF effective index of the loaded CPS waveguide ($n_{RF,l}$) should be as close as possible to the group index of the optical mode ($n_{o,g}$). We achieve this by employing a slow-wave design with T-shaped extensions on the electrodes for increased
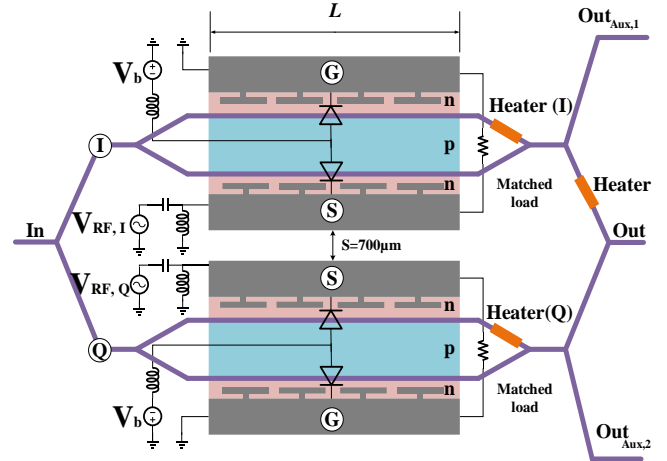

Fig. 1. Schematic of the IQ modulator using SiP TW-MZMs with a series push-pull driving scheme.

the metal capacitance to slow down the RF signal while maintaining a 50-Ω impedance. The CPS transmission lines are designed following the previously reported procedure [13] with the geometric parameters detailed in Fig. 3a. The bandwidth of the MZM is dominated by the RF propagation loss in the p-n junction loaded CPS [13]. More details on the RF loss are given pin Appendix. The TW electrode is terminated by an on-chip 50-Ω load implemented using n-doped silicon.

B. RF Characteristics of Fabricated Device

We had the TW-MZM design in Figs. 1 and 2 fabricated at IME. We measured the small-signal frequency response using a 67 GHz Keysight network analyzer for two bias voltages, 0 V and -0.75 V. After removing the effects of the RF probes, cables and unloaded section of the transmission line, we extracted the RF parameters including propagation loss, effective index and input impedance of the transmission line.

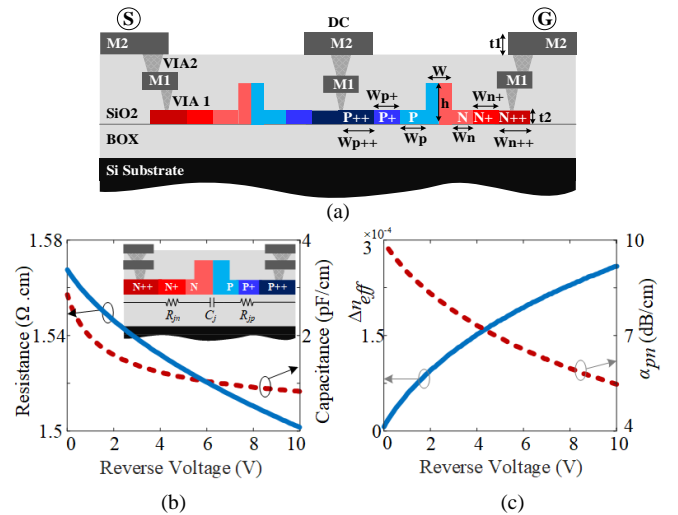Figure 3b presents the microwave effective index as a

Fig. 2. a) Cross-section of lateral P-N junction waveguide with (all dimensions in μm) Wp++ = 5.2, Wp+ = 0.83, Wp = 0.37, Wn++ = 5.2, Wn+ = 0.81, Wn = 0.39, W = 0.5, h= 0.22, t1 = 2, t2 = 0.09, b) resistance and capacitance of the lateral pn junction vs. reverse bias voltage, and c) Δn_{eff} vs. reverse bias voltage for the lateral pn junction in (a).
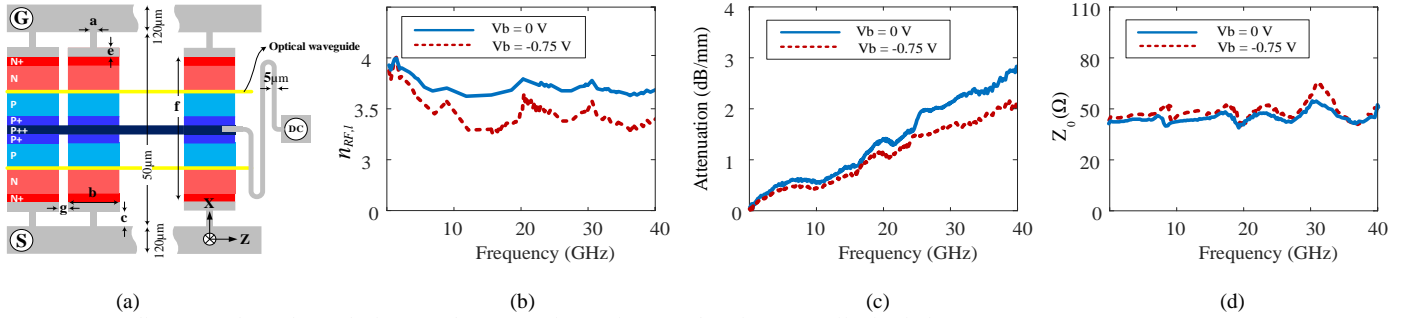
Fig. 3. a) Traveling wave electrode employing "T" shape extensions to increase the microwave effective index. a =2, b = 47, C = 9, e = 10, f = 12.5 and g = 3 (all dimensions in μm). Measured results for b) microwave effective index for the TW electrode when it is loaded by a pn doped silicon wave-guide, c) microwave attenuation along the TW electrode and d) characteristic impedance of the TW electrode loaded by p-n junction.

function of frequency. We can see that at 30 GHz it changes from 3.67 to 3.5, as the bias voltage V_b changes from zero to -0.75 V, respectively. Despite this variation, these values are close to the optical group index of the silicon waveguide, 3.89, found via simulation. The microwave loss per unit length in the loaded CPS is presented in Fig. 3c. This loss is the combination of the loss in the metallic electrode and the dielectric loss in p-n junctions. For higher frequencies, it is dominated by the dielectric loss in the doped silicon. More details regarding the contributions of various RF loss sources are presented in appendix. Figure 3d shows the characteristic impedance of the loaded transmission line. We achieved good 50-Ω impedance matching for up to 30 GHz.

III. OPTIMIZATION FOR QAM

There are three major sources of power penalty in SiP modulators: optical loss of the phase shifter, modulation loss due to the relatively small driving voltage swing compared to V_π, and ISI penalty due to the limited bandwidth of the modulator. All of these impairments degrade the eye opening at the output of modulator, which leads to lower margin for detection hence, higher bit error rate. In this section, we use a numerical model of the design in section II to illustrate these contributions.

Using the parameters extracted in Section II, we build a model of the IQ modulator in Lumerical Interconnect, where the bandwidth impact due to the RF loss and velocity mismatch was included as a filter effect on the driving signal applied to the instantaneous response of the modulator [11]. Analysis of back-to-back data transmission is then performed in Matlab. We assume I and Q arms to be identical without loss imbalance, and that their phase difference is always 90º. This assumption neglects any phases drift between I and Q data.

For push-pull operation at the null point, we use the change in refractive index, Δn_{eff}, in Fig. 2c, to find the phase shift induced by input voltage V_{in}, given by

$$\Delta\varphi(V_{in}) = \left[\Delta n_{eff}\left(V_b + \frac{V_{in}}{2}\right) - \Delta n_{eff}\left(V_b - \frac{V_{in}}{2}\right)\right]\frac{2\pi L}{\lambda} \quad (1)$$

The normalized electrical field output of the IQ modulator is

$$E_{out} = e^{-\alpha L/2}\left(\underbrace{E_0\cos\left(\frac{\Delta\varphi(V_{in,I})}{2} + \frac{\pi}{2}\right)}_{E_I} + i\underbrace{E_0\cos\left(\frac{\Delta\varphi(V_{in,Q})}{2} + \frac{\pi}{2}\right)}_{E_Q}\right) \quad (2)$$

where $E_0 = E_{in}/2$ is the module of the electric fields E_I and E_Q induced by $V_{in,I}$ and $V_{in,Q}$ in the I and Q branches, respectively; α is the optical attenuation loss. We plot in Fig. 4a the normalized output electrical field found from (1) and (2) as a function of input voltage with a swing of V_{RF}. A nonzero optical loss leads to a maximum value below 0.5.

To illustrate the various sources of impairment, we simulate a 16-QAM signal at 30 Gbaud and operate at a bias voltage of one volt. We input a multilevel square pulse to the numerical model and observe the output. We assume a limited rise time of the input, modeled by a first order Gaussian filter with 3 dB bandwidth of 25 GHz. The I branch four level, 16-QAM drive signal at the output of this filter is illustrated in Fig. 4a by the pink inset. The signal swings from -1V to 1V, where we set $V_{RF} = 2|V_b| = 2V$. Note that due to $V_{RF} < 2V_\pi$, we incur a modulation loss, as illustrated.

We show the output multilevel eye in blue in Fig. 4a in an inset. If the modulator had infinite bandwidth, the eye opening would be the distance between rails, as indicated. For this noiseless eye, the reduced eye opening is strictly due to limited bandwidth of the modulator. This leads to an ISI penalty or patterning effect. The penalty depends on the ratio of the modulator's bandwidth over baud rate (BW_{EO}/BR). In this simulation, bandwidth is 25 GHz while baud rate is 30 Gbaud, yielding a ratio of $BW_{EO}/BR = 25/30$.

We produce a two-dimensional scatter plot of the received constellation in Fig. 4b, again assuming identical and balanced I and Q branches. Four sets of constellation points are illustrated. The black points are simulations with no impairments present – the simulator had $\alpha = 0$, $V_{RF} = 2V_\pi$, and no bandwidth limitation. The green points are generated when we next set $\alpha > 0$. Moving from black points to green points shows the impact of optical loss. The red points have $\alpha > 0$, $V_{RF} < 2V_\pi$, and still no bandwidth limitation. We can observe a large impact on the constellation when we move from green dots to red dots – the result of operating at reduced RF swing.
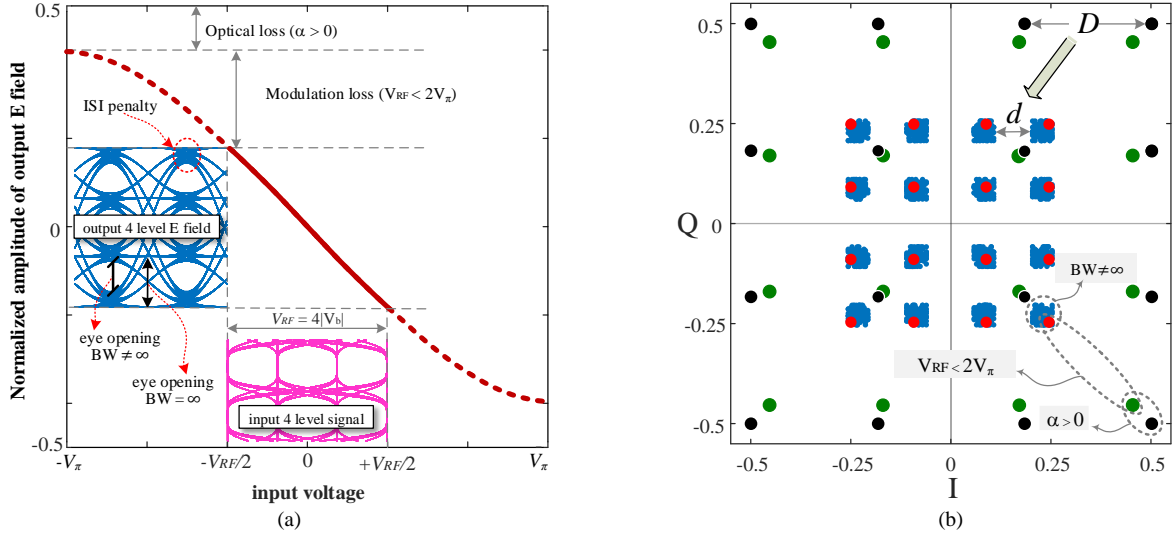
Fig. 4. a) Transfer function of the SiP TW-MZM in one branch (I or Q) operating at the null point. b) Constellation diagram of output data for 16-QAM where constellation points are: black with no impairments, green with only optical loss, red with optical and modulation loss but no ISI, and blue dots are a scatter plot of output four level E field when all three sources of impairment are present. $V_{RF} = 2|V_b| = 2V$, BR = 30 Gbaud, $BW_{E-O} \sim 25$ GHz, $V_\pi \sim 6.4V$, $L = 4.5$mm.

Finally, the collection of blue points is the scatter plot of the output four level signal in Fig. 4a. This includes the bandwidth limitation in the simulator.

1) Interdependencies in impairments

The three penalty sources identified are interdependent. Minimizing one of them does not minimize the total power penalty of the modulator. The penalty induced by each impairments can be traded-off. For example, for a fixed swing of the driving voltage (V_{RF}), decreasing the modulator length decreases the optical loss and increases the electro-optic bandwidth, but it also increases the modulation loss (as a result of increased $V\pi$ and lower extinction ratio of the modulator) and limits the output eye opening. On the other hand, using a longer phase shifter reduces BW_{E-O} of the modulator and increases the total optical loss (αL). Hence, the total penalty from the modulator has to be minimized by simultaneously considering all of the penalty sources.

2) Quantifying modulator power penalty for QAM

The cumulative effect of the three impairments leads to a greatly reduced minimal separation between the constellation points. As illustrated in the upper corner of Fig. 4b, the separation "D" moves to "d". We can use this change in separation to quantify the impact on bit error rate, neglecting impairments in the receiver.

In order to find the optimal length of the phase shifter, we define the modulator power penalty (MPP) as the ratio of the limited clear distance (d) to the ideal value (D), which is proportional to those impairments noted in Fig. 4a

$$MPP = -10\log\left(\frac{d}{D}\right) \propto \left(P_{\alpha L} + P_{ER} + P_{ISI}\right) \quad (3)$$

where $P_{\alpha L}$, P_{ER}, P_{ISI} represent power penalty from the optical loss, modulation loss and the limited electro-optic BW (that causes ISI) of the modulator, respectively as explained in [11[. The output from the IQ modulator is a coherent combination of the two MZMs. As a result, the d is also affected by the impairments that limit the eye opening in each MZM as shown

in Fig. 4a.

We sweep the phase shifter length and examine several bias voltage choices. The RF voltage swings across 2V peak-to-peak; this choice is motivated by the maximum achievable swing by instruments available in our lab. We simulate 60 Gbaud 16-QAM and find minimal separation d numerically. We plot the modulator penalty from (3) in Fig. 5. By examining multiple values of bias voltage, we can determine the relative importance of each penalty source contribution to MPP in(3).

In Fig (5), we observe an optimal length, L_{opt}, for each bias voltage. For phase shifter lengths shorter than L_{opt}, modulation loss is the dominant penalty; for longer lengths, the electro-optic bandwidth is limited, and ISI dominates. Optimal length gets monotonically larger as the reverse voltage increases. This is because a higher bandwidth is available as reverse bias voltage increases, which compensates for the reduction in bandwidth at longer phase shifter lengths. While L_{opt} increases monotonically with bias voltage, the achieved MPP does not. While higher reverse voltage enables higher bandwidth, modulation loss also increases. This trade off leads to minimum MPP that decrease at first, and increase after V_b = -0.75 V.

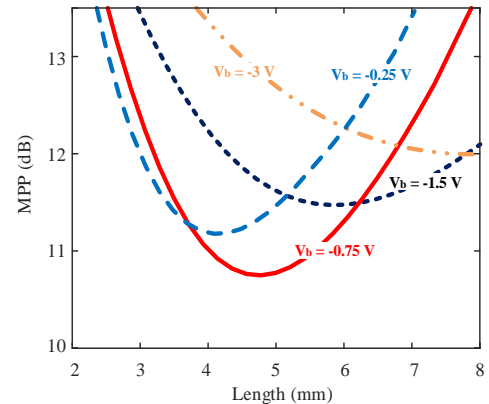From Fig. 5, we identify the optimal combination of the

Fig. 5. Modulator power penalty as expressed in (3) for 16QAM at 60 Gbaud; minimum MPP at V_b=-0.75V and phase shifter length between 4.5 and 5 mm.
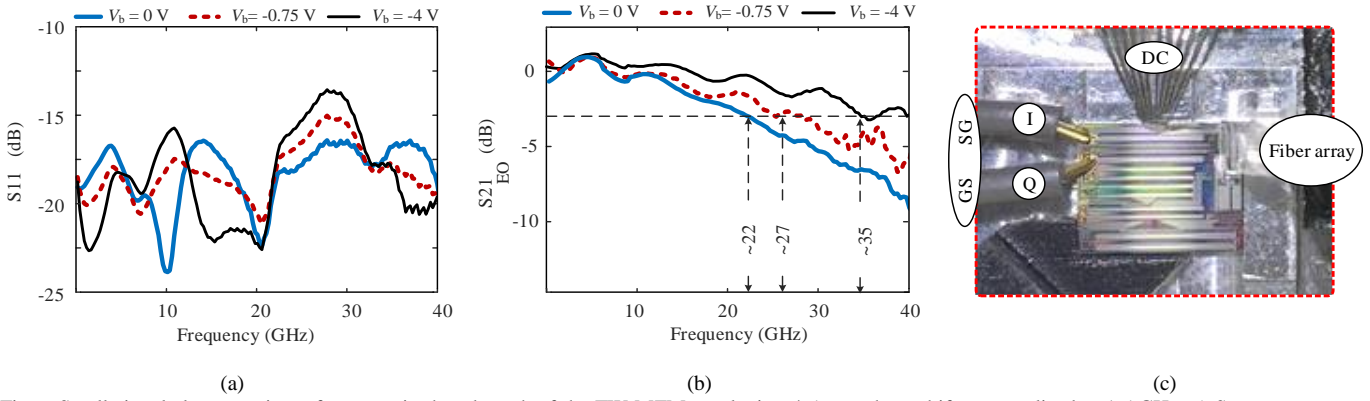
(a)   (b)   (c)

Fig. 6 Small signal electro-optic performance in the *I* branch of the TW-MZM employing 4.5 mm phase shifter normalized at 1.5 GHz: a) S_{11} parameter vs. frequency, and b) S_{21} electro-optic (EO) parameter vs. frequency. c) Photograph of the fabricated TW-SiP IQ modulator in the test setup.

phase-shifter length and bias voltage giving the lowest MPP. For $V_b = -0.75$ V, the overall minimum point is near 4.75 mm, with little change in the range from 4.4 mm to 5 mm. Based on this result, we choose a 4.5-mm-long phase shifter in our IQ modulator design and for fabrication. In modulation experiments presented later, we bias the modulator at -0.75 V.

3) RF crosstalk between I & Q branches

Due to the weak electro-optic effect in silicon, all-silicon TW-MZMs typically are several millimetres in length (4.5 mm in the case examined in this paper). As the *I* and the *Q* branches each require such long TW electrodes, spacing between the branches is critical. If placed too close to one another, unwanted RF modes may be created that affect the overall modulator performance. Specifically, when two CPS transmission lines are too closely packed, the signal and ground of one CPS and the ground of the other CPS form an asymmetric coplanar waveguide (CPW). This causes excess RF loss and crosstalk.

To avoid this unwanted phenomenon, the two MZMs need to be sufficiently separated. Using the RF characteristics extracted in Section II., we perform a 4-port electromagnetic simulation of two 4.5-mm-long CPS transmission lines in HFSS. We found a distance of 700 µm to be a safe design, leading to crosstalk between two adjacent CPS transmission lines that is less than -30 dB in the entire simulation frequency range up to 45 GHz.

IV. EXPERIMENT AND RESULTS

Figure 6c is a photograph of the fabricated SiP IQ modulator in the test configuration. A "GSSG" RF probe is used to the drive the modulator and a DC probe controls the bias voltage and thermal phase shifters. We use a fiber array for optical IO through surface grating couplers. Each of the TW-MZMs (in I and Q branches) is characterized individually through the auxiliary optical outputs (Out$_{Aux1}$, Out$_{Aux2}$ in Fig. 1).

We measured the small signal responses of the MZMs. The Q branch shows slightly better small signal performance than the I branch due to fabrication errors. We present results for the I branch. Figure 6a presents the S_{11} at various bias voltage. We can see that even in the worst case ($V_b = -4$ V) the reflection is still well under -12.5 dB. The 3-dB modulation bandwidth (S_{21}) is measured to be 36 GHz at $V_b = -4$ V (Fig. 6b) and decreases to 27 GHz for $V_b = -0.75$ V. Ripples in the S21 responses are due to imperfect RF connection, e.g., between the RF probe and the metal contact pads on the silicon chip. The average static V_π at $V_b = -0.75$ V is 7.3 V ($V_{\pi\text{-I}} = 7.8$ V, $V_{\pi\text{-Q}} = 6.9$ V). On-chip insertion loss of the IQ modulator is measured to be 6.8 dB. The coupling loss from the fiber array to the SiP chip is 8.5 dB.

A. Data transmission setup

Following characterization, we ran data transmission experiments using the experimental setup in Fig. 7. We use an EDFA to boost a continuous wave carrier at 1530 nm from an external cavity laser (ECL) to 22 dBm before coupling onto the chip. We use on-chip heaters to implement the 90° degree phase shift between the two branches. The TW-MZMs in the I and the Q branches are operated at their null point to maximize the modulation amplitude of the *E* field. We achieve this by adjusting the phase shift between the two arms of each MZM through on-chip heaters, Heater (I) and Heater (Q) in Fig. 1.

To generate 16-QAM, the driving voltages $V_{RF, I}$ and $V_{RF, Q}$ feed two uncorrelated four-level signals to the I and Q branches as shown in Fig. 1. We amplify two outputs of an 84 GSa/s, 8-bit DAC with two SHF 50 GHz, 18 dBm drivers and apply the signal to the modulator using an RF probe. In the transmitter digital signal processing (DSP) before uploading to the DAC, the QAM data is grey mapped from a pseudo random bit sequence (PRBS) of order 19. We apply a pre-emphasis filter to compensate the DAC, RF amplifier and RF probe frequency
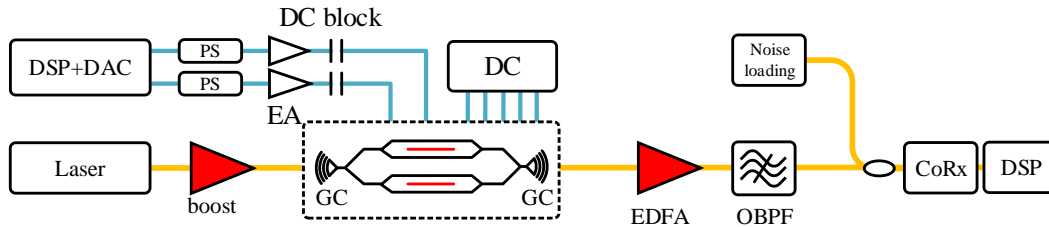

Fig. 7. Experimental setup. PS: phase shifter; DC: direct current; GC: grating coupler; OBPF: Optical band-pass filter.

response. This allows us to investigate the impairment from the modulator. The pre-emphasized symbols are further pulse shaped by a raised cosine filter with roll-off filter of 0.01. RF phase shifters are used to precisely de-skew the I and Q channels. We control the optical operation point of each MZM using the DC probed heaters.

We amplify the modulated optical signal with a two-stage EDFA. We place an optical band-pass filter (OBPF after the second EDFA to reject out-of-band amplified spontaneous emission (ASE) noise. To sweep OSNR, we load the signal with ASE noise at the receiver end. The output optical signal is mixed with a 14 dBm local oscillator (LO) and fed to a 70 GHz coherent receiver (CoRx) formed by a discreet optical hybrid and 70 GHz balanced photodetectors. We use a Keysight real-time oscilloscope (RTO) with a 60-GHz analog bandwidth to sample the output of the CoRx at 160 GSa/s.

B. Experimental characterization for MPP

To verify our design methodology and the numerical model, we experimentally characterize the MPP of the IQ modulator at various bias voltages and compare these measurements with simulation results. Optical loss (P_{aL}) is determined by employing the measured optical loss of the modulator versus applied reverse bias voltage. To estimate the P_{ER}, V_π at different reverse bias voltages are measured; the modulation loss is then calculated for a driving voltage of 2 V_{pp}. The experimental characterization for P_{ISI} requires a more complex procedure that is described as follows.

To quantify the penalty from the bandwidth limitation of the modulator (P_{ISI}), a training-aided channel estimation method is employed. We load the DAC with a Nyquist-16QAM training sequence with a roll-off factor of 0.01, where the frequency responses of the DAC, the RTO and other RF components (such as drivers and RF cables) have been digitally pre-compensated, ensuring a flat spectrum in the driving signal of the modulator. The ISI penalty of the modulator is then estimated following the signal-processing flow shown in Fig. 8a and described in the following text. The data samples are first synchronized and framed via the training sequence. After training-aided frequency offset compensation (TA-FOC), and training-aided carrier phase recovery (TA-CPR), the channel response is estimated by minimizing the mean square error (MMSE). The estimated channel response is averaged over 100 frames to reduce noise and numerical errors. Since no adaptive equalizer is applied, and the frequency responses of other RF components have been de-embedded through the pre-compensation of the training sequence, the obtained MMSE channel response represents the response of the modulator alone.

Using the estimated channel response, we run a post-emulation to visualize the ISI by the convolution of the averaged channel response with an ideal 16QAM signal. The post-emulated 30-Gbaud 16QAM constellations with ISI distortion are shown in Fig. 8b for different reverse bias voltages. Note that the modulator stays in the linear regime for the given voltage swing, thus nonlinear modulation distortion is negligible in this case. Due to the relatively narrow analog
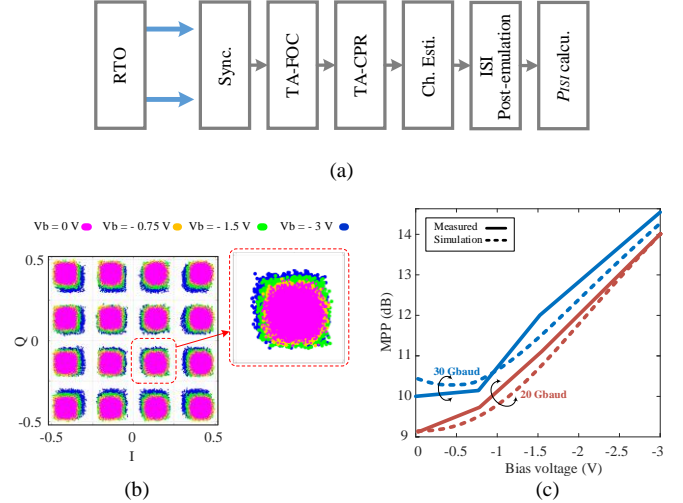

Fig. 8. a) Flow chart of training-aided channel estimation. b) post emulated constellation diagrams of received data for 30-Gbaud 16QAM, when reverse bias voltage changes from 0 V (where the diodes are slightly forward biased) to -3 V. c) simulation and measurement results for MPP versus reverse bias voltage for two different baud rates.

bandwidth (< 20 GHz at -3 dB) of the DAC, the accuracy of the ISI emulation degrades drastically at a higher frequency. Therefore, we have only characterized P_{ISI} up to 30-Gbaud in our verification.

Finally, the total MPP of the modulator under test at different bias voltages are calculated using (3) for 20 Gbaud and 30 Gbaud. The results are shown in Fig. 8c. For the lower baud rate (i.e., 20 Gbaud), the electro-optic bandwidth of the modulator is sufficiently wide even at zero bias (~22 GHz in Fig. 6b) with little ISI penalty. In this case, the total MPP increases as the reverse bias voltage due to the higher V_π and thus higher modulation loss. However, for the higher baud rate (i.e., 30 Gbaud), P_{ISI} becomes dominates the power penalty from modulation loss (P_{aL}) at zero bias. Increasing the reverse bias to 0.75 V achieves the minimum MPP thanks to the best trade-off between the bandwidth (~27 GHz in Fig. 6b) and the modulation loss, as discussed in the previous section.

As shown in Fig. 8c, the simulation results match very well with the measured MPP. Although the MPP can only be accurately measured at a relatively low baud rate due to the narrow bandwidth of the DAC used in our experiment, the same reasoning applies at higher baud rates. Hence, we are confident the simulation results shown in Fig.5 present the optimum modulator design for 60-Gbaud 16QAM modulation. In the following, we will present data transmission results to evaluate the system-level performance of the designed modulator.

C. BER performance

Experiments are run at 60 Gbaud (240 Gb/s) for three different bias voltages. The BER performance of 16-QAM with an RF voltage swings across 2V peak-to-peak is shown in Fig. 9a. Two forward error correction (FEC) thresholds are indicated: a 7% overhead FEC threshold at BER = 3.8e-3, and a 20% overhead FEC threshold at BER = 2.4e-2.

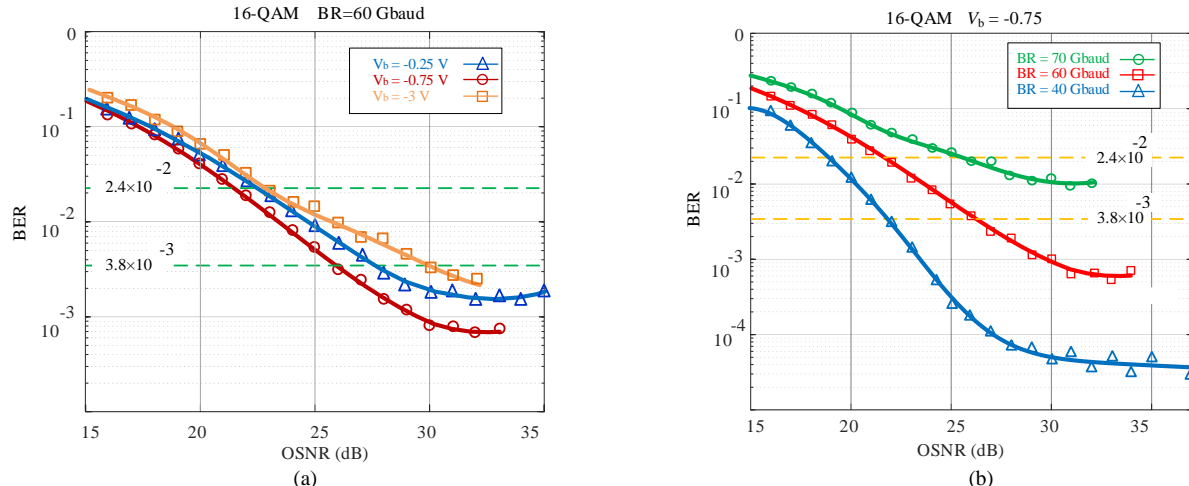In Fig. 9a, we observe that increasing the bias voltage from

Fig. 9. a) BER performance for different reverse bias voltages at 60 Gbaud. b) BER performance for 40, 60, and 70 Gbaud 16-QAM when the 4.5-mm-long phase-shifter is biased at V_b = -0.75V.

V_b = -0.25V (where with $V_{RF} = 2$ V_{pp}, the series-connected diodes are slightly forward biased, but the current passing through them is still negligible) to -0.75 V significantly improves the BER performance of the modulator. In this case, the bandwidth achieved from stronger reverse bias of the phase shifter compensates the modulation loss penalty due to higher V_π at V_b = -0.75 V. The MPP simulation predicted this behaviour, as shown in Fig. 5. Lower MPP (Fig. 5) indicates a larger clear distance between the constellation points, leading to better BER performance. Pushing the phase shifter to stronger reverse bias reduces the highest achievable OSNR due to a lower modulation efficiency. We also notice that V_b = -3V shows the worst BER of all the three curves in Fig. 9a despite the highest bandwidth. This extra OSNR penalty was also observed in another work [15] where the optical modulator with a higher bandwidth showed a worse OSNR sensitivity due to a higher V_π (i.e., higher modulation loss). We suspect this is related to dynamic nonlinear behavior that requires further examination in future work.

The MPP calculations are based on ideal, theoretical predictions for the effects of modulation loss and ISI. In practical systems, several typical measures are taken to overcome these effects, including optical amplification and digital signal processing for channel equalization. The residual impact of modulation loss and ISI (despite countermeasures) cumulatively determines the BER performance. Our simulations of MPP capture the best design/operating point in ideal systems. Our experiments do the same for residual effects when employing best known methods to optimize system performance. The results in Fig. 9a confirm that the trend observed in the MPP simulations predicts relative performance in practical systems. Therefore, our design tool, though idealized, is effective for optimization. It is not surprising that designing a system to avoid the requirement for extreme compensation (either in the form of high amplification to overcome small extinction ratio, or equalization to avoid very narrow bandwidth) leads to practical advantages. Operating the

system in more benign scenarios give greater chance of success to mitigation techniques. Hence, our MPP tool is effective in designing the modulator even though based on theoretical models that do not directly reflect the experimental scenario.

We further investigate the achievable baud rate of the modulator. Figure 9b shows the BER at 40, 60 and 70 Gbaud when the reverse bias voltage is V_b = -0.75 V and the RF voltage swings across 2V peak-to-peak. A large margin is available at 40 Gbaud. The BER performance is below the 20% FEC threshold up to 70 Gbaud (net bit rate of 224 Gb/s). A 400 Gb/s dual-polarization transmitter can be achieved by integrating on the same chip two IQ modulators, a polarization rotator (from TE to TM) and a polarization combiner.

V. CONCLUSION

We have experimentally demonstrated an integrated IQ modulator based on a SiP foundry process. Our results show that all-silicon modulators have great potential for high-baud-rate coherent optical communications systems. We demonstrated that the performance of the SiP IQ modulator can be effectively optimized by minimizing the modulation-induced power penalty in an optical transmission link. The design and operation of the TW-MZMs were optimized for 16-QAM at 60 Gbaud. The experimental results verified our theoretical prediction. This system-orientated optimization methodology can also be used in other contexts with various modulation formats and rates. Using the SiP IQ modulator, we have achieved single-polarization 16-QAM at 60 Gbaud (BER at the 7% FEC threshold) and at 70 Gbaud (BER below the 20% FEC threshold), giving a net data rate of 224 Gb/s and 233 Gb/s, respectively. This indicates a promising solution for 400+ Gb/s dual-polarization transmitter. Note that these results were achieved without pre-compensating for the impairments from the modulator. More sophisticated digital or optical pre-emphasise could be done to overcome the limitations of the modulator and further push the bit rate.

APPENDIX

RF LOSS IN THE TRANSMISSION LINE

Assuming quasi-TEM propagation, we use the telegrapher's RLGC model [12-14] to investigate the slow-wave propagation of microwaves along the CPS transmission line on SOI. The RLGC model of the p-n junction loaded CPS transmission line is shown in Fig. 10. The two p-n junctions connected in series (Fig. 2a) are modeled by a combination of the junction capacitance C_j and resistance $R_{pn}=R_{jp}+R_{jn}$, as labeled in Fig. 2b. The parallel equivalents of the junction capacitance and conductance per unit length C_{tpn} and G_{tpn} are given by:

$$C_{tpn} = \frac{C_{pn}}{1+R_{pn}^2.C_{pn}^2.\omega^2} \tag{4}$$

$$G_{tpn} = \frac{R_{pn}.C_{pn}^2.\omega^2}{1+R_{pn}^2.C_{pn}^2.\omega^2} \tag{5}$$

Applying the low loss approximation, the p-n junction loaded characteristic impedance Z_{0l} and propagation constant γ_l are given by

$$Z_{0l} = \sqrt{\frac{L_{cps}}{C_{cps}+C_{tpn}}} \tag{6}$$

$$\gamma_l = \frac{1}{2}(\underbrace{\frac{R_{cps}}{Z_{0l}}}_{\substack{conductor\\loss}} + \underbrace{\left(G_{cps}+G_{tpn}\right)Z_{0l}}_{dielectric\ loss}) + j\omega\underbrace{\sqrt{L_{cps}\left(C_{cps}+C_{tpn}\right)}}_{\frac{n_{RF\_l}}{c_o}} \tag{7}$$

where R_{cps}, L_{cps}, C_{cps} and G_{cps} are the resistance, inductance, capacitance, and conductance per unit length of the un-loaded CPS transmission line, respectively. Note that C_{cps} includes the capacitive coupling through the oxide layer and the silicon substrate capacitance.

The major sources of the RF loss are the conductor loss, α_{TL}, and the dielectric loss in the doped silicon of the pn junction, α_{pn}. The conductor loss can be expressed as

$$\alpha_{TL} = \frac{1}{2}\left(R_0 + R_\delta\sqrt{f}\right)\sqrt{\frac{C_{cps}+C_{tpn}}{L_{cps}}} \tag{8}$$

where R_0 is the DC resistance and R_δ is the frequency-dependent resistance due to the skin effect in the CPS transmission line. Assuming the conductance of the un-loaded CPS transmission line is small, the dielectric loss can be approximated as

$$\alpha_{pn} = \left(\frac{R_{pn}.C_{pn}^2.\omega^2}{1+R_{pn}^2.C_{pn}^2.\omega^2}\right)\sqrt{\frac{L_{cps}}{C_{cps}+C_{tpn}}} \tag{9}$$

According to (8) and (9), the conductor loss increases as the square root of frequency, while the dielectric loss increases much faster. The dielectric loss increases quadratically with frequency for relatively small frequencies, i.e., when $R_{pn}.c_{pn}^2.\omega^2 \ll 1$ or, in other words, when the frequency is much smaller than the cut-off frequency of the p-n junction (typically in the range of 60 to 100 GHz).

Based on equation (9), reducing the p-n junction capacitance can significantly decrease the RF loss. The series push-pull
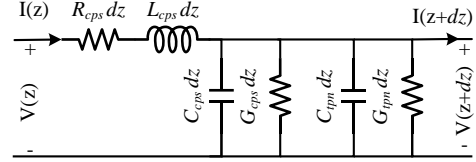

Fig. 10 Telegrapher's RLGC model of the p-n junction loaded CPS transmission line. The top view of the transmission line is illustrated in Fig. 3a
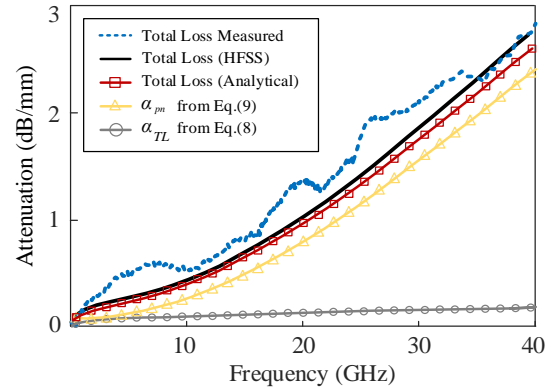

Fig. 11 Measured and simulated microwave attenuation of the MZM. Gray and yellow colored solid lines present the loss predicted using (8) and (9), respectively. The black colored solid line and blue colored dotted-line present the total microwave loss from HFSS simulation and measured device. Red colored solid line shows the total loss predicted by the analytical solution. These results are captured when $V_b = 0$ V.

driving scheme reduces the overall capacitive load of the p-n junction by about 50%.

The microwave loss of the series push-pull p-n junction-loaded CPS transmission line (Fig. 3a) is investigated numerically using HFSS, analytically using (8) and (9), and also measured experimentally. The results presented in Fig. 11 show that the dielectric loss from the p-n junction is the dominant source of the total microwave attenuation; the contribution of (8) is negligible above 10 GHz. The total loss predicted by the analytical solution (summation of (8) and (9)) is also plotted in Fig. 11. When $C_{pn} = 3.1$ pF/cm (slightly higher than 2.8 pF/cm as predicted in Fig. 2 for $V_b = 0$ V), the total loss predicted by the analytical solution is in a good agreement with the results predicted by HFSS simulation.

REFERENCES

[1] Milosevic, Milan M., Stevan Stanković, Scott Reynolds, Thalía Domínguez Bucio, Ke Li, David J. Thomson, Frederic Gardes, and

Graham T. Reed. "The emergence of silicon photonics as a flexible technology platform." Proceedings of the IEEE, vol. 99, pp. 1-16, 2018.

[2]   Shi, Wei, Yelong Xu, Hassan Sepehrian, Sophie LaRochelle, and Leslie A. Rusch. "Silicon photonic modulators for PAM transmissions." *Journal of Optics*, vol. 20, no. 8, p. 083002, 2018.

[3]   Xiong, Chi, Douglas M. Gill, Jonathan E. Proesel, Jason S. Orcutt, Wilfried Haensch, and William M. J. Green. "Monolithic 56 Gb/s silicon photonic pulse-amplitude modulation transmitter." *Optica*, vol. 3, no. 10, pp. 1060-1065, 2016.

[4]   H. Sepehrian, A. Yekani, L. A. Rusch and W. Shi, "CMOS-Photonics Codesign of an Integrated DAC-Less PAM-4 Silicon Photonic Transmitter," in *IEEE Transactions on Circuits and Systems I: Regular Papers*, vol. 63, no. 12, pp. 2158-2168, Dec. 2016.

[5]   Shiyu Zhou, Hsin-ta Wu, Khosrov Sadeghipour, Carmelo Scarcella, Cormac Eason, Marc Rensing, Mark J. Power, Cleitus Antony, Peter O'Brien, Paul D. Townsend, and Peter Ossieur, "Optimization of PAM-4 transmitters based on lumped silicon photonic MZMs for high-speed short-reach optical links," *Opt. Express* 25, 4312-4325 (2017).

[6]   Li, Miaofeng, Lei Wang, Xiang Li, Xi Xiao, and Shaohua Yu. "Silicon intensity Mach–Zehnder modulator for single lane 100 Gb/s applications." Photonics Research, vol. 6, no. 2, pp. 109-116, 2018.

[7]   P. Dong, C. Xie, L. L. Buhl, Y. K. Chen, J. H. Sinsky and G. Raybon, "Silicon In-Phase/Quadrature Modulator with On-Chip Optical Equalizer," *IEEE Journal of Lightwave Technology*, vol. 33, no. 6, pp. 1191-1196, March15, 15 2015.

[8]   Kazuhiro Goi, Akira Oka, Hiroyuki Kusaka, Yoshihiro Terada, Kensuke Ogawa, Tsung-Yang Liow, Xiaoguang Tu, Guo-Qiang Lo, and Dim-Lee Kwong, "Low-loss high-speed silicon IQ modulator for QPSK/DQPSK in C and L bands," *Opt. Express,* vol. 22, pp. 10703-10709, 2014.

[9]   C. Y. Wong, S. Zhang, Y. Fang, L. Liu, T. Wang, Q. Zhang, S. Deng, G. N. Liu, and X. Xu, "Silicon IQ Modulator for Next-Generation Metro Network," IEEE *Journal of Lightwave Technology*, vol. 34, no. 2, pp. 730-736, 2016.

[10] Ding, Jianfeng, Sizhu Shao, Lei Zhang, Xin Fu, and Lin Yang. "Silicon 16-QAM optical modulator driven by four binary electrical signals." *Optics letters*, vol. 42, no. 8, pp. 1636-1639, 2017.

[11] H. Sepehrian, A. Yekani, W. Shi and L. A. Rusch, "Assessing Performance of Silicon Photonic Modulators for Pulse Amplitude Modulation," *IEEE Journal of Selected Topics in Quantum Electronics*, vol. 24, no. 6, pp. 1-10, Nov.-Dec. 2018.

[12] H. Bahrami, H. Sepehrian, C. S. Park, L. A. Rusch and W. Shi, "Time-Domain Large-Signal Modeling of Traveling-Wave Modulators on SOI," *IEEE J. Lightwave Technol.* vol. 34, no. 11, pp. 2812-2823, 2016.

[13] David Patel, Samir Ghosh, Mathieu Chagnon, Alireza Samani, Venkat Veerasubramanian, Mohamed Osman, and David V. Plant, "Design, analysis, and transmission system performance of a 41 GHz silicon photonic modulator," *Opt. Express* 23, 14263-14287 (2015).

[14] J. Witzens, T. Baehr-Jones, and M. Hochberg, "Design of transmission line driven slot waveguide Mach-Zehnder interferometers and application to analog optical links," in *Opt. Express 18*, 16902-16928 (2010).

[15] J. Zhou, J. Wang, L. Zhu, Q. Zhang, and J. Hong, "Silicon Photonics Carrier Depletion Modulators Capable of 85Gbaud 16QAM and 64Gbaud 64QAM," in OFC 2019.